Progress in Physics of Applied Materials 6 (2026), Serial Number 12, 205-215

Semnan University

Progress in Physics of Applied Materials

journal homepage: https://ppam.semnan.ac.ir/

High-Performance Solar Cells Systems with ZnO+ Spiro-OMeTAD Perovskite- NiO layers

Khadeeja Mhoder H. Alshami [a], Ali Bahari [a*], Addnan H. Al-Aarajiy [b]

[a] *Department of solid state Physics, University of Mazandaran, Babolsar, Iran*
[b] *Department of Applied Medical Physics, University of Hilla, Babylon, Iraq*

ARTICLE INFO

Article history:
Received: 9 December 2025
Revised: 25 December 2025
Accepted: 26 December 2025
Published online: 27 January 2026

Keywords:
Electron transport layer (ETL);
Perovskite solar cells;
Spiro-OMeTAD;
Carrier mobility;
Hysteresis loop.

ABSTRACT

Achieving a suitable electron-transporting layer for balancing electron- hole numbers, and the accumulation of electrical charges at HTL/anode interface layer, remains a key challenge for perovskite-organic solar cells (PSC) application. Here, ZnO, NiO, and spiro- OMeTAD (SOT) as electron-transporting layers (ETLs)/ perovskite/ SOT as hole-transporting layers (HTLs) of PSC have been widely analyzed. To find better ETL- materials in PSCP systems for balancing the difference between electron- hole (e-h) diffusion distance, and acting as a hole barrier material for reducing the recombination ratio of e - h at the active layer, Al (cathode), ZnO/NiO+10wt.% SOT as ETL, perovskite-SOT as the active layer, and SOT as HTL and anode layer of PSCP systems are investigated with the help of relevant spectroscopic techniques, home- set electrical systems, ABET Technologies, Sun 2000 solar simulator, and microscopic images. In the ETL layer, ZnO/10% wt. of SOT with zero, 25, 50, 75, and 100 wt.% of NiO particles, shows that sample with 75% NiO particles, with higher carrier mobility (62.5 $cm^2/V.S$), higher power conversion efficiency (PCE= 8.3%), higher fill factor (FF=67%), lower hysteresis loop, and lower SS (1.3 mV/dec.) can be used as desirable ETL for the next PSCP systems.

1. Introduction

Today, the necessity of using clean energy and producing electricity for consumption is obvious to everyone. Everyone has welcomed the use of sunlight and the increasing development of solar cell manufacturing. Every day, reports are presented to increase the efficiency of solar cells and use different materials for this purpose. photovoltaic systems - solar cells (PSC) can be called the most important of these solar cells. Today, industries and manufacturers of advanced solar cells are giving great attention to the enhancement of advantages and elimination of defects in photovoltaic solar cells through perovskite (PSCP) systems. Although many studies [1-5] have studied and fabricated solar cells with silicon elements, PSCP is a desirable alternative solar cell due to its advantages such as higher efficiency. The clear reason for using perovskite-based compounds instead of silicon (despite the cheapness and abundance of silicon) was that most of the light received in silicon solar cells was reflected from their surface and less was absorbed.

To find higher efficiency (with lower electron (e)- hole (h) recombination, and better charge transport layers (CTLs), many workers [6-10] have reported that higher power conversion efficiency (PCE), PSCP devices can be achieved with using suitable HTL (hole transport layer) and ETL (electron transport layer) layers to get a lower recombination rate of e-h in the active- perovskite layer. For this purpose, spiro-OMeTAD (SOT) or 2,2′,7,7′-Tetrakis (N,N-di-p-methoxyphenyl-amine)-9,9′-spirobifluorene (O;oxygen,Me: methyl groups and TAD: triaryldiamine, which refers to the N,N-di-p-methoxyphenylamine moiety),

* Corresponding author.
E-mail address: a.bahari@umz.ac.ir

Cite this article as:
H. Alshami, K.M., Bahari, A. and H. Al-Aarajiy, A., 2026. High-Performance Solar Cells Systems with ZnO+ Spiro-OMeTAD Perovskite- NiO layers. *Progress in Physics of Applied Materials*, *6*(3), pp.205-215. DOI: 10.22075/ppam.2025.40003.1190

as a HTL, has been widely used in PSCs. Also, ZnO (n-type semiconductor, E_g=2.97 eV direct band gap energy, and work function of 4.45-5.13 eV) with a good visible light transmittance, dissolution process, environmental- friendly, more stable wurtzite and zinc blende phases, optical modulator wave-guide and photonic crystal structure shows a good ETL layer behavior [8, references therein]. However, despite to its high electron mobility (μ_e)=205-300 cm^2/V.s, refractive index=2, Real component of dielectric = 8.5, as ETL layer, it has large band gap energy and an extremely unstable ZnO/perovskite interface layer [8]. When it used as ETL layer and other p-type semiconductor materials such as NiO (nickel oxide), or SOT and some others are used as HTL layers (with hole carrier), the obtained results related to Fill Factor (FF), electron- hole (e-h) balance, Power conversion efficiency (PCE), high accumulation of electrons at the active layer (which is located between ETL and HTL layers), subthreshold swing (SS) and hysteresis loop of the PSCP systems, failed to satisfy the manufacturers of clean energy systems and alternative electricity generation. The reason could be due to unbalance of the recombination rate of electron (e)- hole (h) in the active perovskite layer (Electrons in ZnO-ETL can move faster than hole carriers in the Spiro-OMeTAD -HTL), which may cause aggregation and/or pinch-up on transportation channel, and less output current density.

People have tried to solve PSC problems by using some other materials [11-17], like Spiro-OMeTAD (SOT) and NiO materials as promising hole transporting material, HTLs, for stable PSCs. But, SOT- HTL layer also suffered from instability and doping-induced hygroscopicity, and NiO with lower electric conductivity and the mismatched energy level alignment of NiO_x could not fill this gap. These points caused people [15-20] to suggest changing ETL, HTL, and active layers with some composite, hybrid, and mixed materials.

In the present work, ZnO and 10% in weight (wt.%) of Spiro-OMeTAD (SOT), named ZSOT, were combined with different concentrations of NiO in a hetero-junction structure as shown in the device architecture with a simple schematic of a solar cell device (Fig. 1), Al (cathode)/ ZSOT+NiO (ETL)/pervoskite (active layer)/ SOT (HTL)/ indium tin oxide (ITO) glass (or Si) (anode) was constructed. ITO glass and silicon substrate were used for measuring optical and electronic parameters, respectively.

In the present work, NiO weight content in the ZSOT was zero, 25, 50, 75, and 100 wt.%, were labeled as X_0, X_1, X_2, X_3, X_4, and X_5 (or X_i, i=1,2,3,4,5), respectively. Their nanostructural, sample surface morphology, hysteresis loop, subthreshold swing (SS) are studied and compared with using some relevant techniques such as XRD (X Ray diffraction) patterns, UV-Vis, FESEM (Field emission scanning electron microscope), HRTEM (high resolution transmission electron microscope), ABET Technologies Sun 2000 solar simulator and home set electrical systems, Prova, GPs 132A. We could study the present sample structure, morphology, crystallite's sizes, phases, subthreshold swing (SS) voltage, absorption (A), optical band gap energy ($E_{g,Optical}$) and Fill Factor (FF), Power conversion efficiency (PCE) of the solar systems. The obtained results indicate that X_3 (50% ZSOT+ 50% NiO ETL) sample respect to other present samples, has higher carrier mobility (62.5 cm^2/V.S), better surface morphology, higher PCE (8.3%), lower hysteresis loop, a lower SS (1.3 mV/dec.) and can be a desirable ETL for future of the PSCP systems.

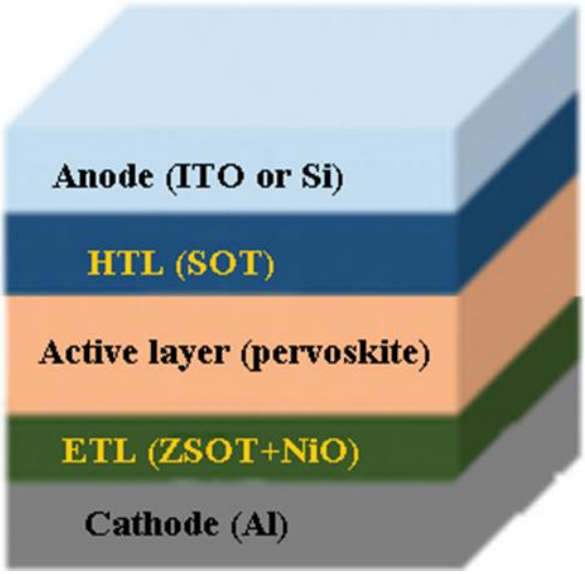

Fig. 1. The device architecture with a simple schematic of solar cell device.

2. Experimental procedures and details

Silicon (Si(100)) and glass substrates are effectively cleaned with H_2SO_4 and chromic solution, and then ultrasonicated with distilled water (20 minutes) to remove any contamination, respectively.

Here, 10% in weight (wt.%) is spiro-OMeTAD (with 2,2',7,7'-tetrakis (N,N-di-p-methoxyphenylamine)-9,9'-spirobifluorene [9, 11] has been used. 90% of the sample composition consists of the sum of zinc oxide (ZnO) and nickel oxide (NiO). For simplicity, the samples based on NiO percentage content are labeled. Xi (0%, 25%, 50%, 50%, 75%, 100% NiO are named X_1, X_2, X_3, X_4, and X_5, respectively).

After that, they were transferred into the solutions containing 200 mg of methyl ammonium iodate, 1 ml of dimethyl formamide, 0.1 ml of dimethyl sulfoxide, 0.5 g of lead iodide, 1 ml of dimethyl formamide and 0.1 ml of dimethyl sulfoxide. Then 0.5 g of lead iodide, 0.2 g of methyl ammonium iodate were added to the previous solution in a glove box containing nitrogen without the presence of oxygen and water vapor. In parallel, zinc acetate dihydrate, nickel chloride hexahydrate, cetyltrimethyl ammonium bromide (CTAB), and citric acid with using the sol-gel route were also prepared (more details can be found in our published papers [3,7,10]). After this step, the zinc acetatedihydrate (99%Zn $(CH_3COO)_2.2H_2O$) and then nickel chloride hexahydrate (99.95% $NiCl_2$. $6H_2O$) were dissolved in deionized water (DI) separately, in that the obtained zinc oxide, with 0.7 gr spiro-OMeTAD, solved in 20 ml clrobanzan by sol-gel method. and was then poured into the solution prepared above, so that 10% in weight of any present sample was spiro-OMeTAD (with 2,2',7,7'-tetrakis (N, N-di-p-methoxyphenylamine)-9,9'-spirobifluorene [9,11]. Nickel oxide (with 0, 25%, 50%, 75%, 100% NiO content) and ZnO (with 90%, 65%, 40%, 15%, 0% in weight percent; %wt.) were added to 10 ml

citric acid and finally gel-form samples were centrifuged three times using ethanol and deionized water (DI) to remove the impurities. The resultant samples were placed in an oven at 110° C for 2 when these metal salts dissociated in the solution (in this case, a coordination complex forming between the metal cation and solvent or water molecules), they were deposited drop-wise on the silicon (polished n-type Si(100) 2×1 with 2 mm thickness, 10×10 cm^2 surface area, 5 Ohm-cm resistivity) and/or indium tin oxide (ITO) glass substrate with using the spin-coating technique. This layered structure consists of aluminum (Al) as the cathode placed with mask procedure on the spiro-OMeTAD as the hole-transport material, ZnO and NiO as the electron transport layer, and n-type Si(100) 2×1 as the anode. The use of nano structured ZnO and NiO layers in this structure is of particular interest due to their unique optical and electronic properties. Meanwhile, the settings of the spin coating device: rotation time =50 second, rotation speed =4000 rpm, and rotation of acceleration= 4000 rpm/sec. In the end, the homogeneous mixture NiO/ZnO/ spiro-OMeTAD was be transferred to Teflon- linked autoclave which was the positioned into a temperature- programmed hot-air oven.

UV-Vis. in the 200–600 nm wavelength range for absorbance of the sample, and FESEM (field effect scanning electron microscope) for analyzing the surface morphology, HRTEM (high resolution transmission electron microscope), and the other electrical home set systems (Prova, GPs 132A), were used for studying the present sample structure, morphology, crystallite's sizes (D), phases (hkl), subthreshold swing (SS), absorption (A), optical band gap energy, and power conversion efficiency (PCE) of the solar systems.

3. Results and Discussion

3.1.XRD analyses

The sample structure is important, however, while the leakage current is lower for the amorphous structure, in the context of solar cell systems, a structure with better surface morphology and higher mobility is more crucial. Here it is observed in the XRD patterns (Fig. 2) that there is no significant shift in the position of the peaks. In other words, the crystalline phases of the samples have not changed with the change in the amount of nickel oxide (shown the sample structure stability). In addition, in Figure 2a, the XRD spectrum of a sample containing zinc oxide shows that it has a crystalline structure.

The dominated peaks, (hkl)= (110), (200) located at 2θ= 41.8° of X_1, and the (200) located at 2θ= 48.1° of X_5, are used for estimating the crystallite sizes. It is confirmed from JCPDS File No. 80-0075 (for ZnO) and JCPDS File No. 78-0429 (for NiO) that the crystalline structure of ZnO is as hexagonal and NiO is face center cubic (FCC). The XRD peaks at angles 36.8° , 48.1° and 64.5° denote the (111), (200), and (220) planes of NiO, respectively. The peaks attributed to the ZnO structure, which are also visible at angles 30.8° , 31.6° , 33.4° , 41.8° and 62.4° in the XRD pattern, correspond to (100), (002), (101), (110), and (102) reflections, respectively.

The peaks of X_2, X_3, X_4 samples in Figure 2c show no significant diffraction angle shifted demonstrated stability of composite structures. It is clear in Figure 1, no impurity peaks are seen. As shown in Figure 1e of spiro-OMeTAD and using Scherrer equation given by Eq.(1) [18], the crystallite size for X_1 and X_5 samples are 40.5 and 25.1 nm, respectively.

$$D = \frac{K\,\lambda}{\beta\,Cos\,\theta} = \frac{0.9\,(1.54\dot{A})}{(FWHM)Cos\,\theta} = \frac{0.14\,nm}{(FWHM)Cos\,\theta} \qquad (1)$$

Where, FWHM (Full Width at half maximum), θ is diffraction angle. The other sample crystallite size and phase are outlined in Table 1.

As shown in Table 1, the smallest crystallite size (D) is for X_3 (25.1 nm) sample, and according to the Hall-Pach relationship, Eq. 2, [18], the mechanical stability coefficient ($\sigma_{Mechanical}$) of X_3 is higher than that of the other samples.

$$\sigma_{Mechanical} \propto \frac{1}{\sqrt{D}} \qquad (2)$$

In other words, when the crystallite size decreases, the mechanical strength of that structure increases. Sample X_3 has the lowest $\sigma_{Mechanical}$ which means this sample has the most stable mechanical structure. As reported by many researchers [1-10], one of the disadvantages of PSCP is its instability structure, so X_3 can be introduced as an alternative element of the next solar cell system with this perspective. This helps the layer transport electric charge carriers by removing the pinch-up or constriction in their transport path.

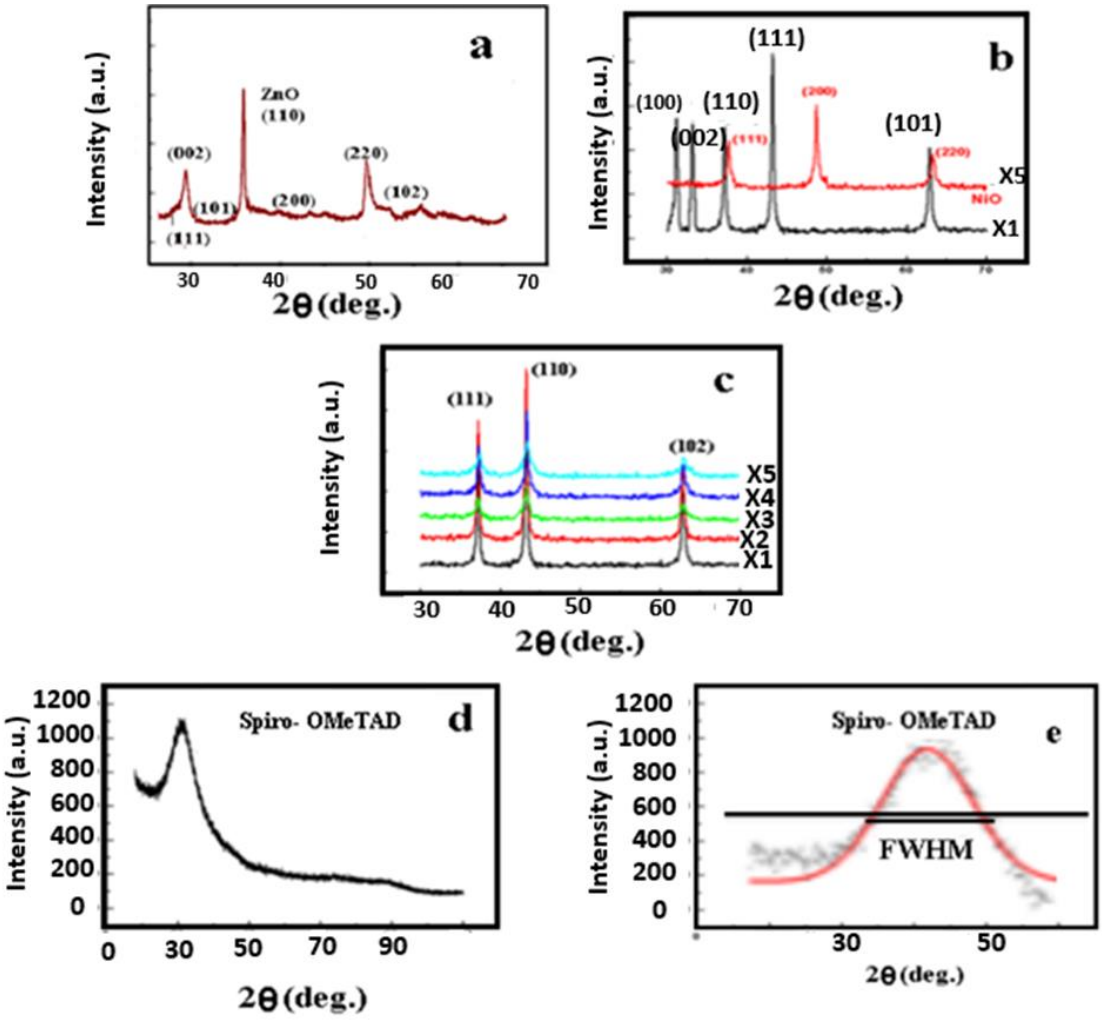

Fig. 2. XRD patterns of (a) ZnO, (b) X_1, X_5, (c) X_1, X_2, X_3, X_4, X_5, (d) spiro-OMeTAD and (e) an example for determining crystallite size, here for Spiro-OMeTAD.

Table 1. Crystallite size and phase of X_1, X_2, X_3, X_4, X_5. Mechanical stability of the sample ($\sigma_{Mechanical}$) is also pointed.

(hkl)	2θ (deg.)	D (nm)	$\sigma_{Mechanical}$
X_1	110	40.5	0.157
X_2	111	36.7	0.165
X_3	110	25.1	0.199
X_4	102	33.4	0.173
X_5	200	29.5	0.184

3.2. UV–Visible spectroscopy analysis

Figs. (3) through (7) display the UV- absorbance spectra of the X_i (i=1,2,3,4,5) samples, obtained in the 190–590 nm wavelength (λ) region. The absorption coefficient (α), optical band gap energies (E_g), Real (ε_{Real}) & imaginary ($\varepsilon_{Im.}$) components of dielectric function and optical conductivity ($\sigma_{Optical}$) of samples were estimated and outlined in Tables (2,3) by using the absorption edge of incoming photon energy (hν) and Tauc relationship.

Absorption (A), reflection (R) and transmittance (T) spectra of the present samples, shown in Figure 3 display that for (λ)> 400 nm, the region of low absorbance and/or higher transmittance (T) for incoming photons appears. Here, extinction coefficient (k) indicates the amount of absorption loss when incoming photons propagate through the sample. Refractive index (n), k, and optical conductivity coefficient (σ) are dependent on the wavelength. The other point is that, X3 sample has higher absorption rate with respect to the other prepared samples, which can cause efficient exciton generation and dissociation, mechanical and environmental stability. It is worth noting that, higher transmittance (See Fig. 4) is desirable for PSCP systems.

The optical band gap energy of samples were estimated by using the absorption edge energy in Figure 5 and using Tauc relationship, given by Eq. (3) [19];

$$(\alpha h\upsilon) = A\,(h\upsilon - E_{g,Optical})^n \quad (3)$$

where, ν is the frequency, h is Planck's constant, A is a constant, and n (Not to be confused with the refractive index) is equal to 1/2 and 2 for a direct and indirect transition, respectively.

Now, we have to find which transition, direct or indirect should be considered for estimating optical band gap energy from UV-vis, absorption spectra of X_i (i=1,2,3,4,5) samples. For PSCP systems and opto- electronic devices, the lower optical band gap energy (here X_3 has lower optical

band gap energy), as well as direct and/or indirect transition is so important.

Before that, let us point aspect ratio and surface plasmon (localized surface plasmon) in this process (more details can be found in [19-21]). Under the excitation of an applied sunlight, nanocrystallites in the present sample may be polarized, generated localized surface plasmons, and even caused negative real part of dielectric functions. In the present thin layer, it cannot travel much (remaining localized in the interface layers). This issue is sensitive to the aspect ratio of a crystallite geometric shape (the ratio of its sizes in different dimensions). In HRTEM images in Figure 8 and also UV-Vis. spectra in Figure 3, the shape of the crystallites is not spherical. We will discuss it in our future study. But some issues need to be pointed.

Our previous works [3, 7, 10, 21] for some other materials demonstrated that UV-Vis. spectra with just one symmetric peak show spherical structure of crystallite; otherwise, two peaks exhibit rod or elliptical shape of crystallite. Here, as shown in Figure 3, at least two dominated peaks are displayed. As shown in TEM images (See Fig. (5)); the geometric structure of the crystallites resembles a rod and/or elliptical shape and is not spherical. The main message of this point, as discussed in details in our previous work [21], we have to consider and discuss the role of surface plasmons as well as the rate of electron-hole recombination and the production/ annihilation of excitons. This point is the reason for X_3 sample performance; it has a lower eflection coefficient (R) and higher transmittance (T).

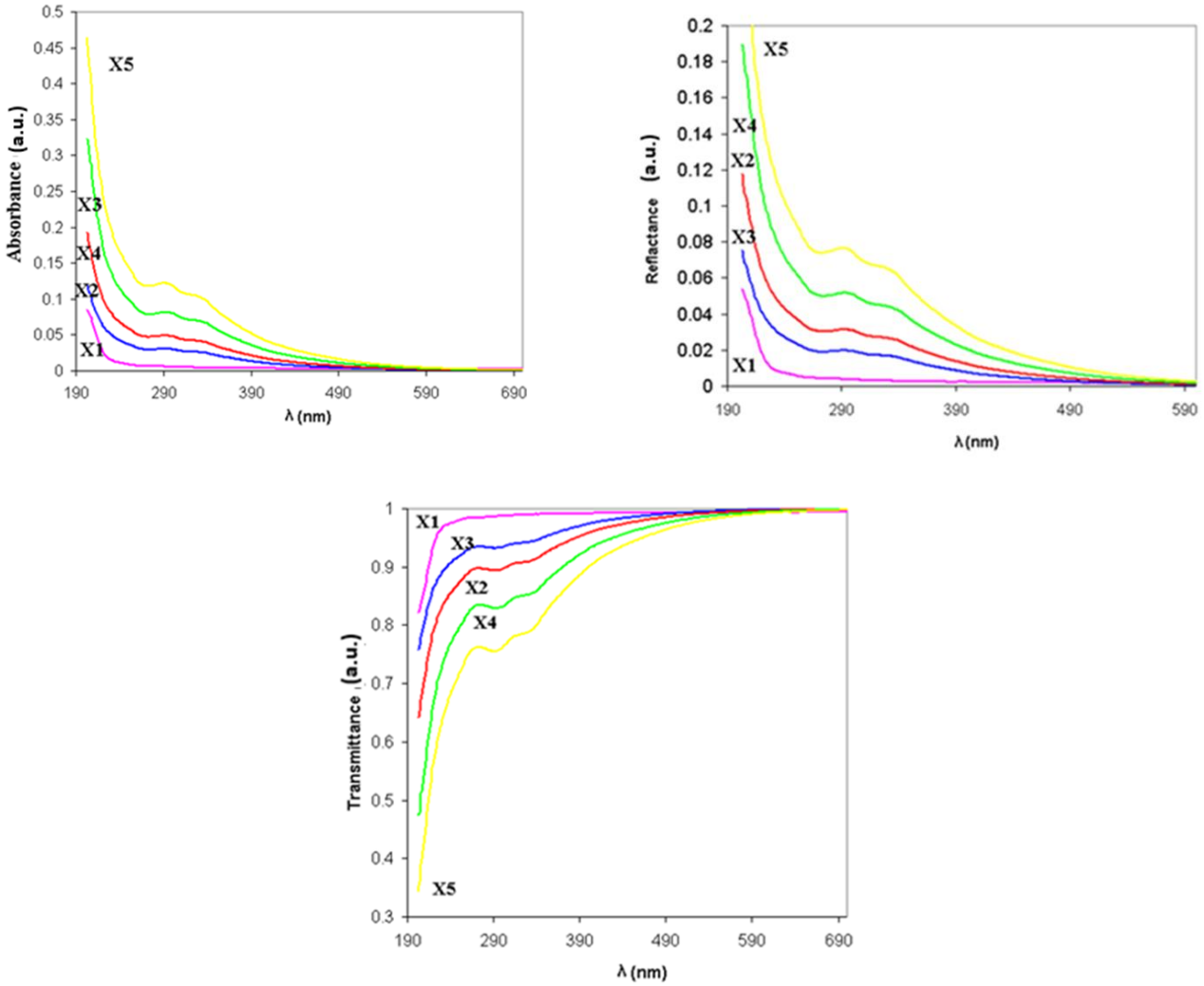

Fig. 3. UV-Vis. spectra of the prepared samples; Absorption (A), Reflection (R), Transmittance (T).

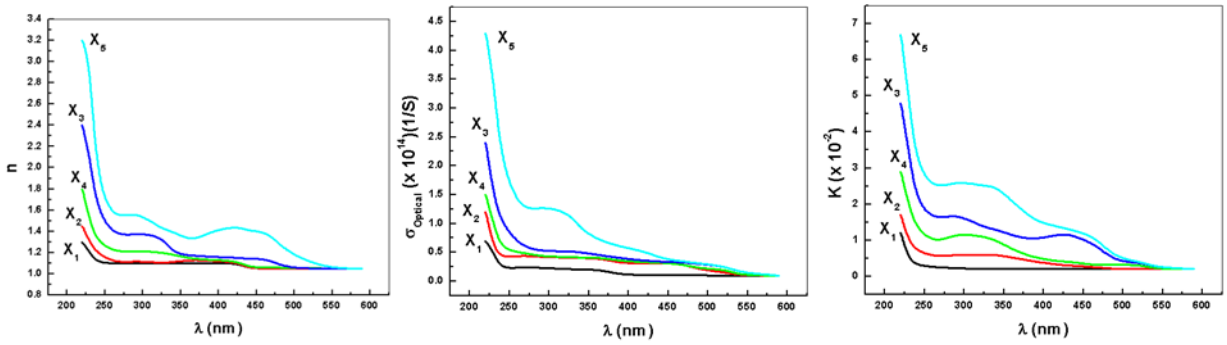

Fig. 4. UV-Vis. spectra of the prepared samples; (Left): refractive index, (Middle): optical conductivity coefficient (σ), and (Right): extinction coefficient (k) versus wavelength. The measurement data are given in Table 2.

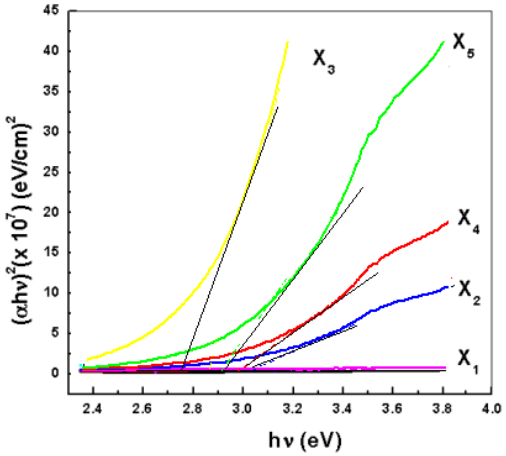

Fig. 5. Optical band gap energy ($E_{g,\,Optical}$) for prepared samples. $E_{g,\,Optical}$ for X_1, X_2, X_3, X_4, X_5 is 3.971, 3.062, 2.705, 2.913, and 2.775 eV, respectively. The lowest optical band gap energy (more charge carrier transitions) is for sample X_3.

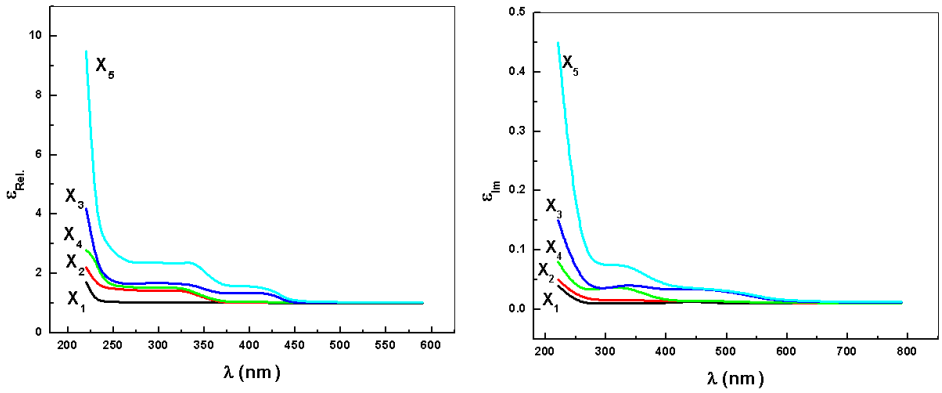

Fig. 6. Real and imaginary component of dielectric function of the prepared samples.

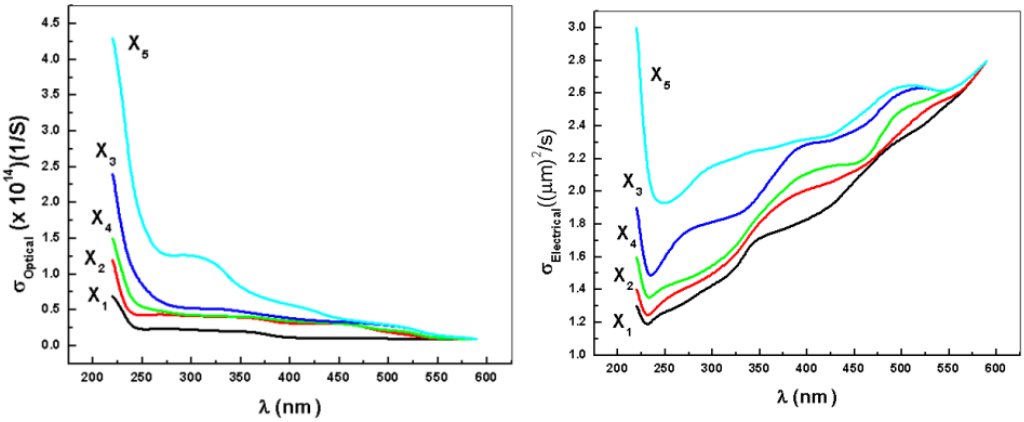

Fig. 7. optical and electrical conductivity of the prepared samples.

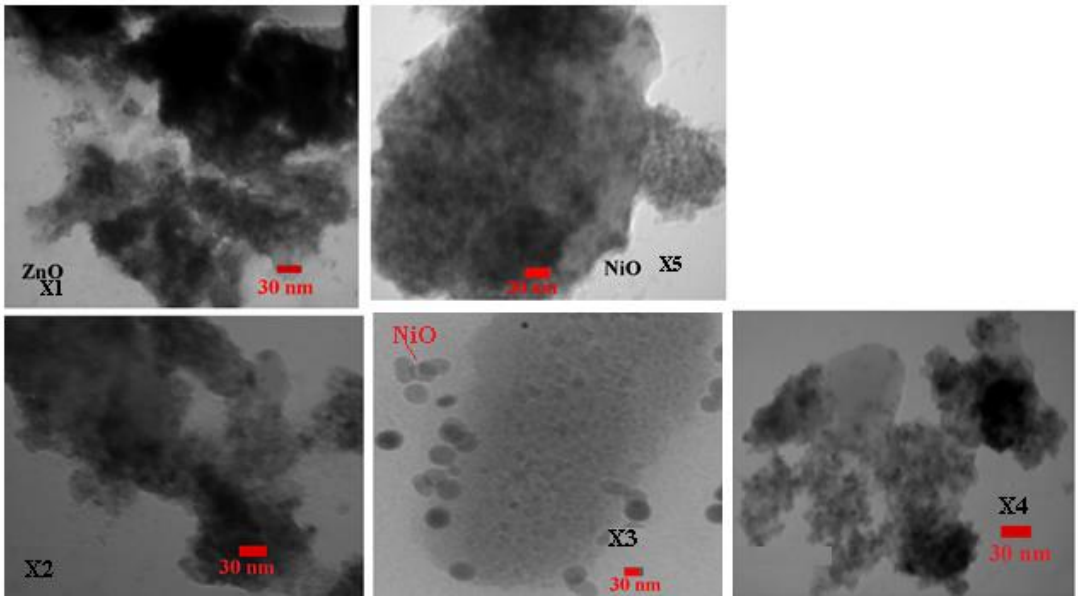

Fig. 8. HRTEM images of the prepared samples. Sample X_3 has no cluster or island structure, which can reduce leakage and tunneling currents.

As reported and discussed in our recent work [19], direct transition and or indirect transition can be distinguished from the relationship of dipole matrix-wavenumber. To find the dipole matrix, we introduced initial ($\Psi_i = \Psi\,(V_{K_i}$; valance band) and final ($\Psi_j = \Psi(V_{K_j}$; conduction band))wave-functions. Since the present samples as ETL and HTL layers of the PSCP devices are semiconductors, here, valance and conduction of energy bands are taken into account. The probability per unit time (W), perturbation term of Hamiltonian (H_1) with $P_{i\to j}$ probability for Ψ_i to Ψ_j transitions of electrons (the same scenario can be done for hole transitions from conduction band to valance band) with absorption of one photon of energy $\hbar\omega$. Neglecting higher order of the vector potential of the electromagnetic field, where Energy $= n\hbar\omega$ and/or $P \propto \frac{\text{Energy}}{unit\ time} = N(q,\omega)\hbar\omega$, from Eq. (4), the net number of transitions per unit time (W) can be found with Eq. (5);

$$< \Psi_{ckj}\left|e^{i(\boldsymbol{q}.\boldsymbol{r})}\,\boldsymbol{e}\cdot\boldsymbol{P}\right|\Psi_{Vki} > = \int \Psi^{*}_{ck\ j(r)}\ e^{i(\boldsymbol{q}.\boldsymbol{r})}\,\boldsymbol{e}\cdot\boldsymbol{P}\Psi_{ck\ i\,(r)}dr \quad (4)$$

Here, by considering modulus of the electronic charge (**e**) and generalized momentum operator (**p**), Fermi distribution function for initial ($f(E_i)$) and final ($f\left(E_j\right)$) occupation states, from elementary many body discussion, we have;

$$\varepsilon(q\&\omega) = 1 + i\frac{2\pi\hbar(mc)^2}{(\omega A_{0)}{}^2 V}N(q,\omega)$$
$$\varepsilon_{Real}(q\&\omega) = 1 - \frac{4\pi}{\omega}\sigma_{Im.}(q\&\omega), \varepsilon_{Im.}(q\&\omega) = \frac{4\pi}{\omega}\sigma_{Real} \quad (5)$$
$$\varepsilon_{Im.}(q\&\omega) = \frac{2\pi\hbar(mc)^2}{(\omega A_{0)}{}^2 V}N(q,\omega) \quad (6)$$

Imaginary component of dielectric function can be determined from real component of the dielectric function with using the Kramers-Kronig relation. Direct transition means that there is no significant rule of phonon, so that for q =0, ω>0, the bipolar matrix ($\boldsymbol{M}_{cv}(K)$); can be found as follow;

$$\boldsymbol{M}_{cv}(K) = < \Psi_{cK}|P|\Psi_{vK} > \quad (7)$$

And;

$$\varepsilon_{Im.}(\omega) = \frac{8\pi^2 e^2}{m^2 V\omega^2}\sum_{CV}\frac{dk}{2\pi}|\boldsymbol{e}.\boldsymbol{M}_{cv}(K)|^2\delta\,(E_{cK} - E_{vK} - \hbar\omega) \quad (8)$$

Therefore, the absorption relation (α(ω)) can be achieved by;

$$\alpha(\omega) = \frac{1}{n(\omega)}\frac{2\pi\hbar C}{VA_0^2\omega}N(q=0,\omega) \quad (9)$$

where $n(\omega)$ is refractive index. As shown in Figures (6,7), the tendency of absorption and imaginary part of dielectric constant for all prepared samples are mostly similar, in that, it is evident from these figures, the optical transitions are direct transitions, since the bipolar matrix ($M_{cv}(k)$) is nearly independent of wave-number (k), i.e. $M_{CV}(k) \simeq constant$. due to nearly homogeneous structures inside the samples, shown in the TEM (Fig. 8), but surface morphology of the samples, shown by FESEM images (Fig. 9), display cluster structure, which can affect on photon scattering processes.

An important point that is evident in the above relationships is related to the crystallite volume, which is inversely related to the absorption coefficient. In other words, the smaller the crystallite volume (The size of crystallite for X_3 (25.1 nm) is smaller than that of other samples), the more incident radiation can be absorbed, which is beneficial for PSCP systems and enhances the efficiency of the solar cell by increasing the amount of absorbed energy (along with a smaller optical band gap energy; 2.25 eV) through increasing electron or hole transitions. Moreover, as shown in HRTEM images (Fig. 8) and also FESEM images in Figure 9, the X_3 sample structure is not cluster or island structure, which can give less

scattering of the particles. In fact, the scattering matrix and their ability to affect the conversion of ultraviolet light to visible light, can also play an important role in the transition of photons of said light to the sample surface, depending on the morphology of the sample surface and the internal structure of the sample. Sample X_3 has better surface morphology (see Fig. 9) and a homogenous structure, both on the sample surface (Fig. 9) and inside the sample (Fig. 8). So, the effect of phonon is less for the X_3 sample and the carrier mobility of X_3 is also higher than those the other present samples. Sample surface with lower roughness can lead to faster carrier mobility (μ), as confirmed with capacitor fabrication with Al/X_i/Si devices (synthesized with solution – spin coating processes), with capacitance per area (C_i (or C)) and $Q = \frac{C(V_{Al-Si}-V_{th})}{wL}$) using probe and GPS 132 A tools and the below equations [7];

$$\mu_{e\ or\ h} = \frac{2l}{wC}\left(\frac{\partial\sqrt{I_{Al-Si}}}{\partial V_{X_i-Al}}\right)^2 \quad (10)$$

Also, subthreshold swing (SS) and carrier mobility (see Fig.10) which have vital rule for solar cell device operation, can be determined from slopping of V_{X_i-Al} –Log I_{Al-Si} (Eq. 11) and $\sqrt{I_{Al-Si}} - V_{X_i-Al}$ curves, Eq. (11), respectively.

$$SS = \frac{dV_{X_i-Al}}{d\ LogI_{Al-Si}} \quad (11)$$

The stability advantage of ZnO+10 wt.% Spiro-OMeTAD+ NiO as ETL with Spiro-OMeTAD, as HTL of the present work. It can exhibit better energy level alignment with the perovskite for efficient charge extraction, with acceptable charge carrier, in that, sample with higher mobility and lower subthreshold swing can allow good extraction, and lower interfacial defects. It can lead consequently to low recombination losses at interfaces, which is a desirable point [9–19].

As shown in Figure 7, there is nearly linear behavior of electrical conductivity function and NiO content, which indirect transition should be taken into account and with considering the second-order perturbation theory, the absorption relation $N(\omega)$ and the join density of states, $J^{indirect}_{\omega_q\ \&\ abs}(\omega)$, are given as follow;

$$N(\omega) = \frac{2\pi}{\hbar}\left(\frac{eA_0}{mc}\right)^2 n_q|C|^2\frac{\Omega}{V}\cdot 2 \cdot\sum_{k_1}\sum_{k_2}\delta(E_{Ck_2} - E_{VK_1} - \hbar\omega - \hbar\omega_q)$$

$$\alpha(\omega,\omega_q) = \frac{8\pi^2e^2n_q}{m^2en\omega}|C|^2\frac{\Omega}{V^2}\sum_{k_1}\sum_{k\_2}\delta(E_{Ck_2} - E_{VK_1} - \hbar\omega - \hbar\omega_q) \quad (12)$$

with $E_{Ck_2} = E_g + \frac{\hbar^2k_2^2}{2m_c^*}, E_{VK_1} = -\frac{\hbar k_1^2}{2m_V^*}, d\boldsymbol{k_m} = 4\pi k_m^2 dk_m,$

$$J^{indirect}_{\omega_q\ \&\ abs}(\omega) = \int_{B.Z}\int_{B.Z}\frac{16\pi^2}{(2\pi)^3(2\pi)^3}\prod_{\boldsymbol{m=1}}^{\boldsymbol{2}} d\boldsymbol{k_m}\ \delta(E_{Ck_2} - E_{VK_1} - \hbar\omega - k_BT) \quad (13)$$

$$J^{indirect}_{\omega_q\ \&\ abs}(\omega) = \frac{(m_V^*m_C^*)^{\frac{3}{2}}}{16\pi^3\hbar^6}\left(\hbar\omega - E_g + k_BT\right)^2\ ;\ \hbar\omega > E_g - k_BT \quad (14)$$

If the dipole matrix element vary linearly with k, the second-class of allowed transitions; $\varepsilon_{2A}(\omega) \equiv \varepsilon_2(\omega)$, Eq. (19) can be appeared;

$$\varepsilon_{2A}(\omega) \equiv \varepsilon_2(\omega) = \frac{A_2}{\omega^2}\left(\hbar\omega - E_g\right)^{\frac{3}{2}} \quad (15)$$

Whilst at the vicinity of the threshold - forbidden transitions; $Eq.(15)$ will be the first-order transitions, given by Eq. (20);

$$\varepsilon_{2F}(\omega) = \frac{A_1}{\omega^2}\left(\hbar\omega - E_g\right)^{\frac{1}{2}}$$
And
$$(\alpha h\upsilon) = A\ (h\upsilon - E_g)^{\frac{1}{2}} \quad (16)$$

Therefore, for nearly direct transition, as shown in Figures (5-7), real (ε_1) imaginary (ε_2) dielectric and optical conductivity (σ) all rise with NiO content, which could be studied in the other research to find the role of excitations and surface plasmon's rules.

3.3. Cell PCE, FF, SS and μ measurements

The main aim of the present work is finding a suitable material for balancing e-h transportation and reducing recombination rate. For this purpose, Fill Factor (FF) and power conversion efficiency (PCE) of the prepared samples with a standardized spectrum (The radiation intensity is 1KW/m^2) are measured with using an ABET Technology Sun 2000 solar simulator. The measurement results are estimated from Eqs. (17, 18) and given in Figure 10 and Table 4, in that current density (I_{mp}, which 0.04 m^2 cell surface area, usually J_{mp}(mA/cm^2) has been used in PCE calculations) and voltage (V_{mp}) at maximum output power are key parameters in this regard. As reported with many researchers [7-15], in PCE calculation using Eq. (18), AM1.5D standard optical condition can be considered, in where for incident photon flux on the cell P_{in}= 1 KW/m^2. In addition, short circuit current density (J_{Sc} (mA/cm^2) and open circuit voltage (V_{oc} (V)) should be also considered for finding Power conversion efficiency (PCE) and Fill Factor (FF), as follow [10]:

$$FF = \frac{V_{mp}\times I_{mp}}{V_{oc}\times I_{sc}} \quad (17)$$

$$\text{PCE} = \frac{V_{oc}\times I_{sc}\times FF}{P_{in}} \quad (18)$$

As shown in Figure 11 (Current Density-Voltage diagram of the cell) and Table 4, it is clear that the cell efficiency is increased after each deposited layer.

Unlike silicon solar cells, which are independent of the hysteresis phenomenon, perovskite solar cells have encountered challenges due to the presence of hysteresis, and the inequality of oxidation and reduction, as well as the exchange and transport of ions. The presence of hysteresis is mostly due to the methylammonium lead iodide halide, surface plasmon [21-23], carrier trapping/entrapment, and ion migration in perovskite structure, which has ferromagnetic characteristics. This issue causes that organic- perovskite photovoltaic and solar cell systems' stability and performance to still suffer from its current density-voltage (J-V) hysteresis, as can be clearly seen from the voltammetry cycle (CV) curves for forward and reverse scans in Figure 11, where sample X_3 has a smaller area

inside the loop. There are many reasons for the existence of a hysteresis loop. Here, it could be due to the ion transpiration in oxidation-reduction processes, where a smaller hysteresis loop (see Fig. 12), could give better oxidation-reduction processes and more output current flux, and of course it is a more desirable conclusion. The X_3 sample is therefore better than the other samples in the present work.

In conclusion, a sample with better and smoother surface morphology, higher mobility, and lower SS (here X_3) can help to reduce the impact of these problems on photovoltaic systems and solar cells. Of course, it is beyond the scope of this discussion, but the presence of more hysteresis is suitable for memristive switching devices.

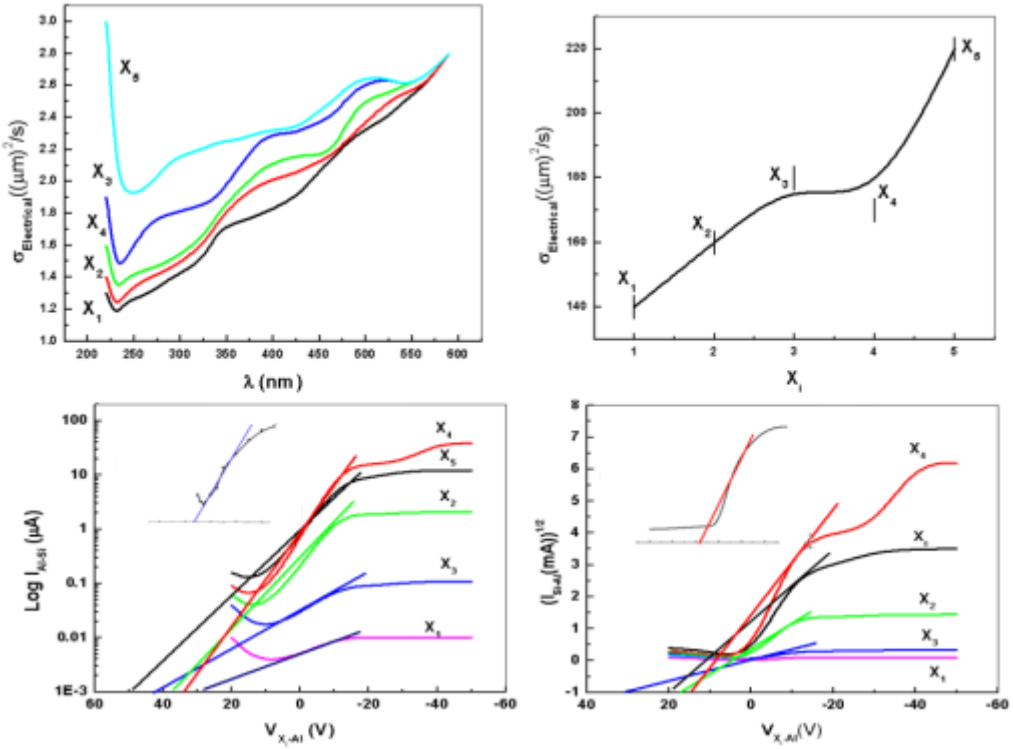

Fig. 10. Carrier mobility, SS, and other electrical conductivity of the prepared samples (Data are given in Tables 2,3).

Table 2. Optical and electrical measurement data of the prepared samples.

Samples	α (10^4)(cm^{-1})	(n)	μ(cm^2/V.s)	SS (mV/decade)
X_1	0.139	1.024	93.8	3.5
X_2	0.174	1.029	40.2	2.5
X_3	0.188	1.036	62.5	1.3
X_4	0.244	1.041	30.1	1.9
X_5	0.278	1.047	25.7	2.8

Table 3. Optical band gap energy, dielectric function components and conductivity parameters for X_1, X_2, X_3, X_4, X_5 samples.

Samples	(ε_{Real})	($\varepsilon_{Im.}$)	$E_{g\text{-}Optical}$ (eV)	$\sigma_{optical}$ $(s)^{-1}$	$\sigma_{Electrical}$ $((\mu m)^2 s^{-1})$
X_1	1.048	0.007	3.971	0.034	140
X_2	1.061	0.009	3.062	0.042	160
X_3	1.047	0.003	2.705	0.069	180
X_4	1.085	0.012	2.913	0.059	170
X_5	1.097	0.014	2.775	0.065	220

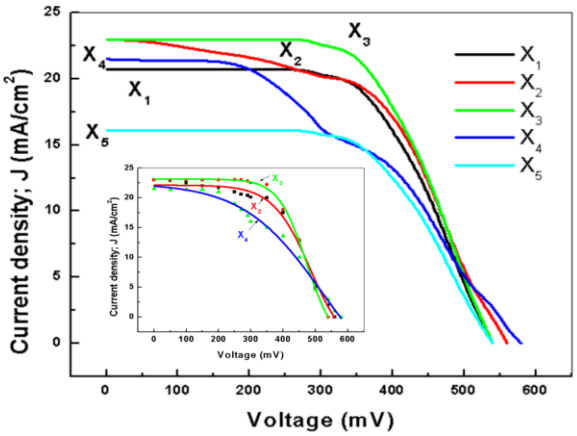

Fig. 11. Current Density-Voltage (J-V) curve of prepared samples (Data are given in Table 4).

Table 4. Solar Cell Parameter measurement data for all samples.

Samples	V_{oc}(mV)	J_{sc}(mA/cm²)	FF (%)	PCE (%)
X_1	587	21	42	5.1
X_2	560	23	55	7.1
X_3	540	23	67	8.3
X_4	580	21.5	43	5.4
X_5	620	18	39	3.5

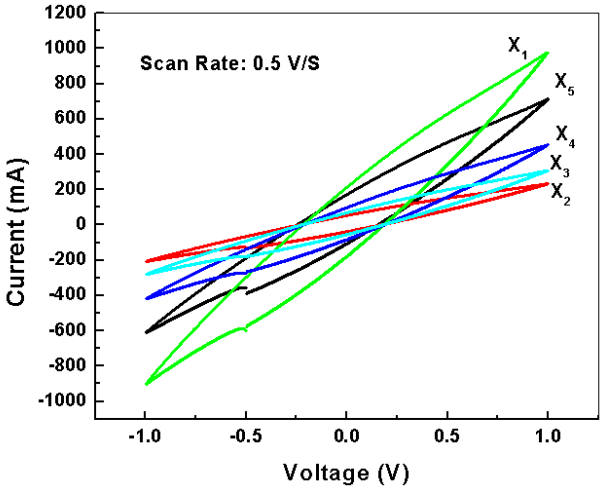

Fig. 12. Hysteresis Loop of all the samples.

4. Conclusions

As discussed above, ETL structure should be modified for balancing the carrier recombination and getting lower subthreshold swing, lower hysteresis and higher PCE. These points are important for the future of organic-perovskite solar cell operations. The reason is that; the presence of hysteresis in perovskite solar cells (PSCs), along with the structural instability of these cells and the great influence of humidity on their durability can reduce FF and PCE. In the above discussions and curves, it has been shown that the sample with 50 wt% nickel oxide with 10% spiro-OmeTAD and 40% zinc oxide had less hysteresis compared to the other samples in the present work, making this sample a suitable candidate for future of the organic-perovskite solar cells generations.

Funding Statement

This research received no specific grant from any funding agency.

Conflicts of interest

The authors declare that they have no known competing financial interests or personal relationships that could have appeared to influence the work reported in this paper.

Authors contribution statement

A. Bahari: Conceptualization, Methodology, Writing–original draft, Formal analysis, Validation, Investigation, Writing–original draft, Supervision. Kh. M. H. Alshami: investigation, data collection, Synthesis, analysis, resources, writing, original draft, and Ad. H. Al-Aarajiy: data collection, Synthesis, analysis, validation.

Data availability statement

All data generated or analyzed during this study are included in this published article.

References

[1] Aulakh, R.K., Singh, G., Pathak, D., Singh, R.I., Mittal, A. and Kohli, R., 2025. A Review on Progresses and Developments in Solar cell Technologies. *Journal of Solar Energy Research*, *10*(3), pp.2501-2521.

[2] Sarvi, M., Ebrahimnaz, R. and Zarei Zohdi, H., 2024. A New High Gain DC-DC Converter for Solar System. *Journal of Solar Energy Research*, *9*(4), pp.2115-2124.

[3] Pérez-Martínez, J.C., Berruet, M., Gonzales, C., Salehpour, S., Bahari, A., Arredondo, B. and Guerrero, A., 2023. Role of metal contacts on halide perovskite memristors. *Advanced Functional Materials*, *33*(47), p.2305211.

[4] Raisa, A.T., Sakib, S.N., Hossain, M.J., Rocky, K.A. and Kowsar, A., 2025. Advances in multijunction solar cells: an overview. *Solar Energy Advances*, p.100105.

[5] Saddam, J. and Jaduaa, M., 2025. Design and Fabrication of a Multi-Junction Hybrid Heterostructure Based on ZnO/CuO/PS/Si for Advanced Optoelectronic Applications. *Journal of Solar Energy Research*, *10*(1), pp.2161-2175.

[6] Cao, F., Zhan, S., Dai, X., Cheng, F., Li, W., Feng, Q., Huang, X., Yin, J., Li, J., Zheng, N. and Wu, B., 2024. Redox-Sensitive NiO x Stabilizing Perovskite Films for High-Performance Photovoltaics. *Journal of the American Chemical Society*, *146*(17), pp.11782-11791.

[7] Bahari, A., 2024. Eco-friendly water-induced lithium oxide/polyethyleneimine ethoxylated as a possible gate dielectric of the organic field effect transistor. *Journal of Materials Science: Materials in Electronics*, 35, pp.1709-1715.

[8] Liu, Y., Zhang, Z., Wu, T., Xiang, W., Qin, Z., Shen, X., Peng, Y., Shen, W., Li, Y. and Han, L., 2025. Cost Effectivities Analysis of perovskite Solar Cells: Will it Outperform Crystalline Silicon Ones? *Nano-Micro Letters*, 17(1), p.219.

[9] Teymoriyan, M., Naderi Saatlo, A. and Salimi, M. 2024. Environmental Aspect of Using a High Step-Up No Isolated DC-DC Converter for Solar Photovoltaic Applications: Life Cycle Assessment Point of View. *Journal of Solar Energy Research*, 9(3), pp.1942-1953.

[10] Asgary, S., Milani M. H., Bahari A., and Mohammadpour R., 2021. Role of BCP layer on nonlinear properties of perovskite solar cell, *Solar Energy*, 213, pp.383-393.

[11] Qureshi, A.A., Javed, S., Akram, M.A., Schmidt-Mende, L. and Fakharuddin, A., 2023. Solvent-assisted crystallization of an α-Fe_2O_3 electron transport layer for efficient and stable perovskite solar cells featuring negligible hysteresis. *ACS omega*, *8*(20), pp.18106-18115.

[12] Alaameri, K.J., 2025. Numerical Analysis of the Performance for a Hybrid Renewable System. *Journal of Solar Energy Research*, *10*(3), pp.2465-2474.

[13] Fara, L., Chilibon, I., Craciunescu, D., Diaconu, A. and Fara, S., 2023. Heterojunction tandem solar cells on Si-based metal oxides. *Energies*, *16*(7), p.3033.

[14] Paul, D., Maiti, S., Prakash, S.D. and Neogi, S., 2022. Bi-functional NiO–ZnO nanocomposite: synthesis, characterization, antibacterial and photo-assisted degradation study. *Advanced Powder Technology*, 32, pp.131-138.

[15] Zhang, W., Cojocaru, L., Tamegai, H., Uchida, S., Nakazaki, J., Bessho, T., Liu, X. and Segawa, H., 2025. NiOx nanoparticles as p-dopants for instant oxidation of Spiro-OMeTAD enabling high-performance and stable perovskite solar cells. *Nano Energy*, p.111499.

[16] Kim, H., Choi, D.S., Na, S.I. and Zong, K., 2021. Synthesis and Photovoltaic Properties of Benzotrithiophene-Based Polymer/Non-fullerene Solar Cells. *Journal of Electronic Materials*, *50*(11), pp.6363-6371.

[17] Cardozo, O., Maia, J., R., Farooq, S., Tostes, B., Stingl, A., Farias, P. and Alves Junior, S., 2025. Zinc oxide nanostructures for third generation solar cells: A comprehensive review. *Solar Energy*, 299, pp.113710-113721.

[18] Shahmiri, M.R., Bahari, A., Rostamian, F. and Khaniani, M.B., 2019. Estimation of lattice strain in metallic oxide–organic material nanocomposite using Williamson-Hall equation. *IJPR*, *15*(3).

[19] Ali, Z.H., Bahari, A. and Alarajiy, A.H., 2024. Investigation the effect of concentration (x) in polyvinyl alcohol (PVA) x/nickel phthalocyanine (NiPc)(1-x) nano composites: Real & imaginary component of permeability and optical conductivity. *Optical Materials*, *148*, p.114862.

[20] Albarrak, A.A., Sowilam, G.M. and Kawady, T.A., 2025. Hybrid renewable energy systems in Saudi Arabia: exploring solar-wind integration with fuel cell hydrogen storage. *Journal of Umm Al-Qura University for Engineering and Architecture*, *16*(2), pp.482-500.

[21] Najafi-Ashtiani, H. and Bahari, A., 2016. Optical and cyclic voltammetry behavior studies on nanocomposite film of copolymer and WO_3 grown by electropolymerization. *Synthetic Metals*, *217*, pp.19-28.

[22] Shajari, D., Bahari, A., Gill, P. and Mohseni, M., 2017. Synthesis and tuning of gold nanorods with surface plasmon resonance. *Optical Materials*, *64*, pp.376-383.

[23] Hoseinzadeh, S., Sahebi, S.A.R., Ghasemiasl, R. and Majidian, A.R., 2017. Experimental analysis to improving thermosyphon (TPCT) thermal efficiency using nanoparticles/based fluids (water). *The european physical journal plus*, *132*(5), p.197.